Single-energy x-ray absorption detection: a combined electronic and structural local probe for phase transitions in condensed matter

1998 J. Phys.: Condens. Matter 10 235

(http://iopscience.iop.org/0953-8984/10/1/026)

J. Phys.: Condens. Matter **10** (1998) 235–253. Printed in the UK PII: S0953-8984(98)87306-2

Single-energy x-ray absorption detection: a combined electronic and structural local probe for phase transitions in condensed matter

A Filipponi†, M Borowski†, P W Loeffen†‖, S De Panfilis†, A Di Cicco‡, F Sperandini‡, M Minicucci‡ and M Giorgetti§

† European Synchrotron Radiation Facility, BP 220, F-38043 Grenoble, France

‡ UdR INFM, Dipartimento di Matematica e Fisica, Università degli Studi di Camerino, Via Madonna delle Carceri, 62032 Camerino (MC), Italy

§ Dipartimento di Chimica, Università degli Studi di Camerino, Via S Agostino 1, 62032 Camerino (MC), Italy

Received 3 September 1997

Abstract. We describe the general principle and prototypical applications of a largely unexploited x-ray absorption technique based on single-energy detection during temperature scans. The present developments take advantage of the highly automated experimental set-ups and unique x-ray radiation characteristics available at third-generation synchrotron radiation sources. The sensitivity of the x-ray absorption cross-section to the local structural order makes it possible to investigate the occurrence of phase transitions. We show that by tuning the photon energy to a spectral feature that is highly sensitive to the sample phase it is possible to follow the occurrence and the characteristics of the phase transition. The sensitivity to the atomic fraction of the sample in a certain phase can be in the 10^{-3} range. The energy tunability can be used to enhance the sensitivity to structural or electronic transformations. Several applications to prototypical cases are discussed in detail, including examples of solid–solid phase transitions, melting and undercooling, melting of binary alloys, impurity melting, and non-bulk phenomena.

1. Introduction

The availability of third-generation synchrotron radiation sources has given rise to new experimental opportunities in the field of x-ray absorption spectroscopy (XAS). The exceptional brilliance of undulator sources and the resulting high photon flux at the sample has made it possible to push the timescale for the collection of a complete extended x-ray absorption fine-structure (EXAFS) spectrum down to the 1 s range [1] using a set-up based on the quick EXAFS (QEXAFS) monochromator operation mode [2]. Even shorter timescales are now available in a dispersive EXAFS set-up where the best time resolution is about 100 μs [3].

Also for more conventional bending magnet sources the new dedicated machines present considerable advantages due the very small vertical emittance and stability. As a result, an excellent energy resolution can be obtained without compromising the high flux by matching the intrinsic widths of low-index Si reflections with the geometrical beam divergence defined by the slits and source. Full width at half-maximum (FWHM) resolutions in the range of

‖ Present address: Oxford Instruments, Accelerator Technology Group, Osney Mead, Oxford OX2 0DX, UK.

0953-8984/98/010235+19$19.50

1/10 of the typical K-edge widths can be reached under normal operation. The stability of the electron orbit contributes to the energy stability of the monochromatic beam. New experimental opportunities arise also from the availability of complex sample environments and automated acquisition systems which allow the thermodynamic state of the sample, defined by the temperature T and pressure P, to be changed. These characteristics are particularly suitable for exploiting techniques based on time-resolved monitoring of the changes in the absorption spectrum as a function of some sample environment parameter.

In the present paper, we describe the experimental apparatus and the general theoretical principles of a largely unexploited single-energy x-ray absorption detection technique that we have recently made operational at the x-ray absorption spectroscopy beamline BM29 of the European Synchrotron Radiation Facility (ESRF). The technique is based on the collection of low-noise absorption scans as functions of a sample environment parameter which is appropriately cycled and controlled by the acquisition system. Here we will focus on the temperature variation, but the technique is suitable for further extensions to the pressure, magnetic field and other parameters which define the thermodynamic state of the sample.

It is well known that the study of the x-ray absorption fine structure (XAFS) provides deep insight into the local structure and electronic properties around selected atomic species. In order to identify the occurrence of phase transitions one has to find the optimal balance between the temperature and energy resolution. For a given incoming flux it is possible to collect complete spectra of N points every ΔT. The extreme limit in which the spectrum is composed of a single energy point allows one to obtain the best temperature resolution $\Delta T/N$ for the same total acquisition time (and signal-to-noise ratio). We believe that for a large number of applications the precise measurement of the absorption coefficient at a single wavelength as a function of temperature is the most appropriate experiment for identifying and studying the occurrence of a phase transition. The tunability and stability of the photon source are essential characteristics. By tuning the photon energy to different x-ray absorption features it is possible to switch the sensitivity from structural to electronic sample properties, thus gaining a wide insight into the physical transformations occurring in the sample as a function of the environmental parameter.

The collection of single-energy time scans is not a new concept, but has seldom been used to probe reaction kinetics. Examples of recent applications include solid-combustion reactions [4] and the Cu reduction leading to the activation of a catalyst [1]. In the present development we focus on the potential interest of this technique for studying phase transitions in condensed matter. In order to establish the reliability of the simple interpretative schemes that we propose, a series of prototypical cases are treated, including solid–solid phase transitions, the melting of pure substances and the melting of binary alloys with a eutectic phase diagram. The technique proves to be an extremely powerful tool for revealing and investigating phase transitions in condensed matter.

The paper is organized as follows. The experimental set-up is described in detail in section 2, while section 3 is devoted to the discussion of the general principles. Finally in section 4 a series of prototypical phase transitions are investigated and a quantitative evaluation of the measurements is performed.

2. The experimental set-up

The present experimental installation is available at the European Synchrotron Radiation Facility (ESRF) x-ray absorption beamline on the bending magnet source BM29. The beamline is equipped with a high-stability fixed-exit double-crystal monochromator with

the possibility of sagittal focusing [5]. The vertical source size is about 50 μm (standard deviation). Primary slits at 28.5 m from the source can be adjusted in the useful range 0.05–2.0 mm of aperture. For a Si(311) crystal at 14.3 keV the smaller slits correspond to FWHM resolving power in the 10^5 range (ten times better than the K-edge core-hole widths). The continuous spectrum of the source allows one to scan over wide energy intervals of several keV with a reasonably constant intensity and stable beam position at the sample. The mechanical imperfections of the coupled rotation–translation motion of the monochromator are corrected by a piezoelectric crystal with a feedback system. The instrument is well suited for collecting high-quality XAFS spectra for a wide range of edges from about 4 keV to over 40 keV.

A variety of sample chambers covering the temperature range 20–3000 K are currently available. In particular the beamline is equipped with a closed cycle two-stage He cryostat which operates in the 20–450 K range and a sample chamber for high-temperature experiments up to 3000 K based on a published design [6]. In this high-temperature oven the sample is inserted in an x-ray-transparent resistive crucible and is heated by the Joule effect in high-vacuum conditions. The temperature read-out is achieved with a combination of contact and non-contact probes including chromel–alumel, Pt–Pt:10%Rh and W:5%Re–W:26%Re thermocouples and a small-spot pyrometer probe (1000–3000 °C). Under favourable conditions simultaneous measurements from both the pyrometer and a suitable thermocouple probe are performed and the read-out is recorded in the acquisition system together with the absorption measurement. The temperature is regulated by adjusting the input power and it is possible to obtain an excellent stabilization during long acquisitions as well as to perform programmed ramps with slopes at rates ranging from 100 K s^{-1} to 0.01 K s^{-1}.

With these set-ups it is possible to study phase transitions occurring between 20 K and 3000 K at fixed pressure in the range 0–1 bar. Planned future installations include sample environment chambers with the possibility of independently varying the pressure and temperature in order to probe interesting regions of the P–T diagram. The feasibility of studies in the range 300–1000 K and up to 6 GPa using the Paris–Edinburgh large-volume high-pressure cell [7] has recently been demonstrated during users' beamtime. The examples reported in the following sections will be focused on phase transformations occurring as a function of temperature.

3. Single-energy x-ray absorption detection

3.1. The general principle

The x-ray absorption coefficient of a homogeneous sample with constant thickness d is given by $\alpha = \sigma\rho d = \sigma\rho_s$ where σ is the x-ray absorption cross-section, ρ is the density of the atoms in the sample and ρ_s is the resulting surface density. In the presence of a first-order phase transition the absorption coefficient is expected to change discontinuously. There is a trivial discontinuity due to the change in the sample density ρ which reflects into ρ_s. This produces a discontinuous change of α over the whole energy range. The likelihood of seeing such a density discontinuity is strongly related to the nature of the sample: for bulk samples like foils, $\Delta\rho_s/\rho_s = \Delta\rho^{2/3}/\rho^{2/3}$, while for samples contained in a fixed-thickness container like a cell for liquids, $\Delta\rho_s/\rho_s = \Delta\rho/\rho$. For droplet samples like those used for high-temperature measurements of solid and liquid matter [6] the sample particles change their volume during phase transitions but ρ_s is mainly governed by the volume of the embedding matrix. In the case of porous pellets of graphite or ceramic powder, ρ_s

remains constant and is largely independent of the sample density ρ; therefore, at the phase transition, $\Delta\rho_s = 0$. This property also has a non-negligible advantage in improving the quality of the data collected in typical high-temperature x-ray absorption spectra. In fact, the basic insensitivity to density changes results in large tolerances as regards the temperature stability during the measurement. For comparison, in the case of most fluids, which have large thermal expansion coefficients, relative temperature stabilities in the 10^{-4} range are required to avoid the introduction of spurious noise in a ρ-sensitive sample geometry.

More relevant to the present discussion are the discontinuous changes in σ corresponding to the change in the local structure around photoabsorbing atoms. These are particularly evident in the energy region close to inner-shell x-ray absorption edges. When the phase transition is accompanied by a change of the electronic density of unoccupied states close to the Fermi energy an edge shift occurs which can be detected with very high sensitivity. The discontinuity in σ at a phase transition reflects non-trivial physical effects and can yield insight into the specific structural and electronic transformations.

Let us consider the simplest case of a phase transition from phase 1 to phase 2 occurring at $T = T^\star$. The identification of the most sensitive energy points for the observation of the transition is performed by measuring high-quality x-ray absorption spectra below and above $T^\star$ and by taking the difference. On tuning the photon energy to one of these points, and on scanning the temperature through $T^\star$, it is expected that one will observe a sudden change of the absorption level from α_1 (for phase 1) to α_2 (for phase 2) and vice versa on the cooling stroke. Any departure from this simple behaviour (apart from trivial experimental artifacts) is representative of an interesting physical phenomenon.

A sharp instantaneous discontinuity at $T^\star$ is only obtained in the case of first-order phase transitions characterized by fast dynamics and an absence of overheating (or undercooling) phenomena and for high-purity samples composed of bulk particles. An example of this is the melting of pure substances and this will be discussed extensively in section 4. In the presence of metastable phases, phase 1 can survive above the transition temperature $T^\star$ (or vice versa) and a complete cycle will result in a hysteresis $\alpha(T)$ loop. Above $T^\star$, phase 1 is unstable and will transform eventually to phase 2.

In several cases the transformation takes place in a finite temperature interval of phase coexistence. A single-energy x-ray absorption detection experiment provides, in these cases, a very accurate determination of the relative atomic fraction of the sample in each phase, as a function of temperature. That is, the atomic fraction of phase 1, $f_1(T)$ is directly calculated from the measured absorption coefficient $\alpha(T)$ as

$$f_1(T) = (\alpha(T) - \alpha_2)/\Delta\alpha \qquad \text{with } \Delta\alpha = \alpha_1 - \alpha_2. \tag{1}$$

Considering that typical figures for $|\Delta\alpha|$ and for the noise level in the absorption measurement are 0.1 and 10^{-4} or better, respectively, it is seen that an excellent sensitivity (in the 10^{-3} range) in the determination of f_1 can be obtained. This is an excellent figure for microscopic samples potentially under extreme conditions for which very few alternative probes can be used.

We point out that the technique applies to crystalline phases as well as to disordered phases (liquids). This information can hardly be obtained with such accuracy with other structural techniques. For example the precise determination of the relative fraction of a given crystalline phase from powder x-ray diffraction during a solid–solid phase transition is hampered by the continuous change of size and orientation of the crystallites which is reflected in large spatial and temporal intensity changes in the diffraction rings.

Thus, we propose exploiting such single-energy x-ray absorption detection experiments as functions of a sample environment parameter to investigate the occurrence and nature of

phase transitions in condensed matter. Sensitivity to either electronic or structural properties can be tuned by varying the photon energy. The experimental set-up described in section 2 is ideal for performing such experiments since it permits one to cycle the temperature freely around a phase transition at the desired rate.

It can be argued that more information on the phase transition can be gained by collecting a complete spectrum for every temperature point rather than by measuring the absorption coefficient at a single energy point. This is, in principle, feasible using a dispersive EXAFS set-up in a few milliseconds per spectrum [3] or on a conventional set-up in a few seconds using a quick-EXAFS mode [2]. The problem is that of a balance between temperature resolution, noise level and energy extension. The single-energy technique represents a very useful extremum where all of the incoming photons are used to achieve a very fine temperature resolution ($\approx$0.1 K) and high phase sensitivity due to the lower statistical noise with respect to that achievable by collecting a full spectrum in the same time. This technique can be naturally combined, on the same instrument, with the other extremum which is conventional EXAFS spectroscopy. This allows one to characterize the phase transition and to prepare the sample in the desired state on which a complete structural characterization can be successively obtained by EXAFS and/or x-ray diffraction at a fixed temperature.

3.2. Experimental artifacts

The most critical experimental problems arise from the temperature homogeneity and measurement. In the classical geometry [6] the sample is surrounded on three sides by the x-ray-transparent heating crucible assumed to be at constant temperature. The fourth side is narrow and left open to allow access for the thermocouple. The thermocouple contact is usually placed between the sample and an insulated spacer just above the beam path. Due to the small wire size (usually 125 μm) it is only a minor perturbation to the temperature field. The pyrometer probes the surface temperature of the crucible at the beam level. The coincidence of the two probes (usually within 10 K) guarantees temperature homogeneity and the correctness of the measurement.

A distribution in the sample temperature may arise from longitudinal inhomogeneities along the crucible [6] (the hotter part being in the middle) or from the upper aperture where a small side of the sample faces a low-temperature surrounding. For thick samples this may produce a slightly cooler inner part and slightly hotter surfaces. In the general case, what matters is the sample temperature distribution $\phi(T)$ calculated for the absorbing atomic sites along the beam path. The measured absorption curve $\alpha_{meas}(T)$ is given by the convolution of the ideal curve with the temperature distribution

$$\alpha_{meas} = \phi * \alpha. \tag{2}$$

All practical cases are in two main categories: either there is a temperature gradient across the sample or there is an extremum. In the former case the temperature distribution is uniform and a step discontinuity at a transition is transformed into a linear rising profile with a finite slope; the width of the profile corresponds to the width of the temperature distribution. In the case where an extremum is present, the temperature distribution is characterized by an inverse-square-root singularity on one side. The resulting $\alpha_{meas}(T)$ function is smoothed by a dependence $\sim\sqrt{(T - T^{\star})}$ on one side of the transition. These characteristic behaviours can be easily identified in test systems and appropriate improvements of the homogeneity can be made. In general it is not difficult to reduce the temperature spread below 1 K even for wide samples. The possibility of operating with

a small beam also greatly reduces such experimental difficulties, virtually eliminating any detectable temperature inhomogeneity.

A second experimental artifact can arise from the thermal time constants involved in the system. In the heating phase the crucible is hotter than the sample and the temperature gradient required for the heat transfer can be non-negligible. This puts a limit on the maximum heating or cooling rates that can be reasonably produced under equilibrium conditions. Favourable conditions are usually obtained thanks to the small sample mass, typically 100 mg, with time constants of the order of 1 s. Geometries and shapes can be optimized for specific requirements.

4. Applications

4.1. Solid–solid phase transitions

The prototypical solid–solid phase transition that we consider is the well known transition from b.c.c. (α-Fe) to f.c.c. (γ-Fe) which occurs in pure Fe at $T_{\alpha\leftrightarrow\gamma} = 1185$ K [9].

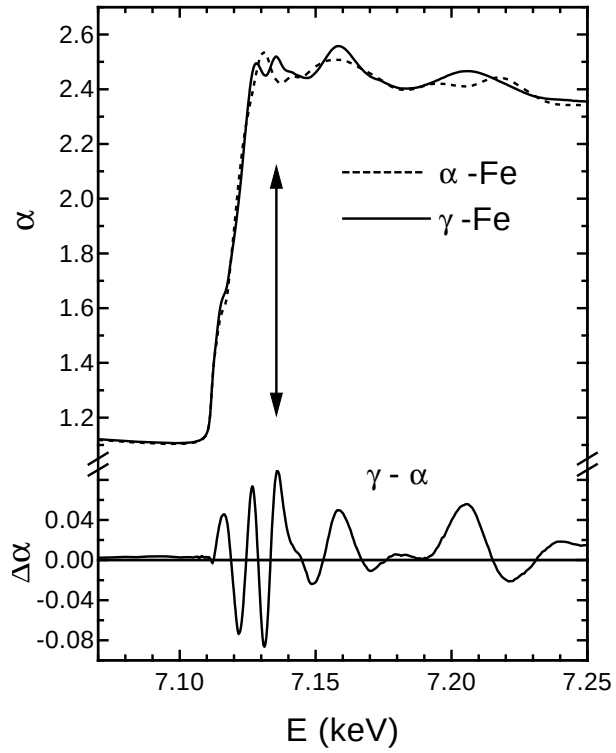

Figure 1. The Fe K edge for a 5 μm Fe foil measured in the α-Fe and γ-Fe phases at $T = 1143$ K and $T = 1218$ K respectively. The arrow indicates the highly phase-sensitive point chosen for the single-energy scans.

We have measured the Fe K-edge x-ray absorption coefficient of an Fe foil 5 μm thick inserted between two BN spacers below ($T = 1143$ K) and above ($T = 1218$ K) the $\alpha \leftrightarrow \gamma$ transition temperature. The measurements over a wide energy region around the Fe K edge are reported in figure 1 together with the difference spectrum. The transition is

accompanied by a density increase of about 1%; this is reflected in the pre-edge region as a slight increase of the absorption level. For a quantitative analysis of this effect, the specific volume $\Omega = 1/\rho$ [10] can be linearized in the vicinity of the transition region as follows:

$$\Omega_\alpha = 5.238\,15 \times 10^{-4}\ T + 11.4755 \tag{3}$$

$$\Omega_\gamma = 1.284\,55 \times 10^{-3}\ T + 10.4531 \tag{4}$$

where T is in K and Ω in Å^3.

Following the previous discussion in section 3, one expects a change of the absorption $\Delta\alpha/\alpha = \Delta\rho^{2/3}/\rho^{2/3}$. Between the temperatures of the two measurements we find a difference $\Delta\rho/\rho = 4.7 \times 10^{-3}$ and $\Delta\rho^{2/3}/\rho^{2/3} = 3.1 \times 10^{-3}$. From considering the fact that at the Fe K edge the absorption coefficient below the edge is about 0.14 times the edge discontinuity, which is about 1.3 in the present case, we expect an absolute absorption discontinuity of $\Delta\alpha = 0.6 \times 10^{-3}$. The density effects can be minimized, in the present case, by taking two temperature values for which the density is the same—for instance, 1070 K and 1232 K—or maximized by choosing the temperatures closer to the transition temperature.

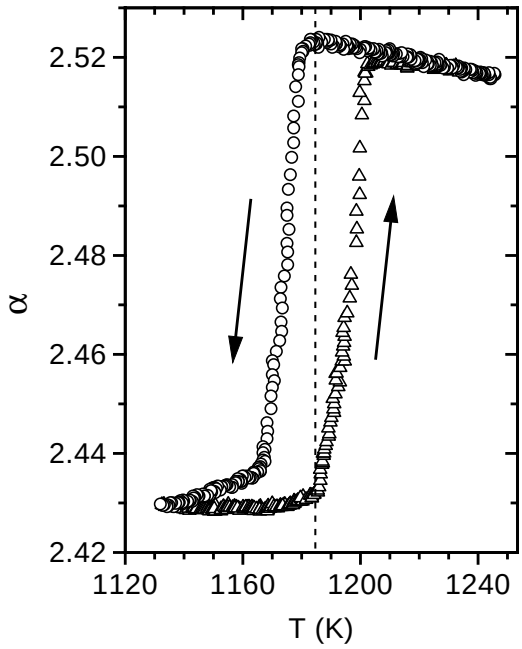

Figure 2. The single-energy x-ray absorption experiment on Fe foil performed at $E = 7.135\,85$ keV. The hysteresis of the transition is quite evident.

The difference spectrum in figure 1 shows several energy points which are highly sensitive to the transition both at the rising edge and in the EXAFS region. The former clearly reflect more the changes in the electronic density of unoccupied states while the latter region directly reflects structural changes. We have performed a temperature scan at fixed energy choosing one of the high-sensitivity points at $E = 7.135\,85$ keV corresponding to the third maximum in the difference spectrum; here the discontinuity is about 7% of the K-edge absorption jump. The results are reported in figure 2. The transformation from α-Fe to γ-Fe occurs, as expected, around $T_{\alpha\leftrightarrow\gamma}$. The complete phase transformation occurs

in a temperature interval of a few degrees and it is possible to stop the temperature ramp at intermediate points to follow the kinetics of the transformation. The clear hysteresis loop is about 20 K wide and it is well reproducible in successive heating cooling cycles as are the details of the absorption curve. It is well known that the Fe $\alpha \leftrightarrow \gamma$ transition is characterized by a small hysteresis [11] whose magnitude strongly depends on the sample purity and morphology [12]. A slight carbon contamination with a gradient through the foil depth profile, arising from the graphite crucible, should also be taken into account to explain the observed broadening of the transition discontinuity in the present case.

This example shows the insight that can be gained into a solid–solid phase transition by the present x-ray absorption technique. For the specific case of the Fe $\alpha \leftrightarrow \gamma$ transition it is clear that a more detailed study can be undertaken to provide further experimental evidence to enrich the present debate on the transformation mechanisms [13].

4.2. Melting and undercooling

Melting of pure substances is associated with a discontinuous change in the absorption coefficient whose intensity mainly reflects the amount of change in the short-range environment. Two representative extreme cases have been considered [8]: that of Ag where the change in the short-range structural order, from an f.c.c. solid to a close-packed liquid, is small, and that of Ge where dramatic changes of the bonding, structural and electronic properties occur. The latter case is investigated in more detail in this paper.

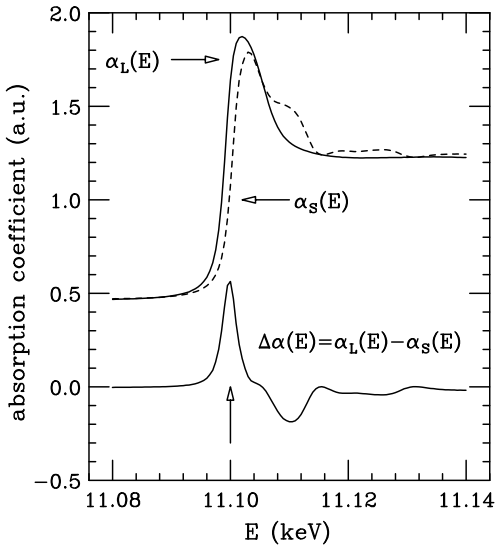

Figure 3. The K edge of solid (α_S, dashed curve) and liquid (α_L, solid curve) Ge at 330 K and 1370 K respectively. The spectacular edge shift and shape change is generated by the semiconductor-to-metal transition. The highest-sensitivity point for melting and metallization is indicated by the vertical arrow on the $\Delta\alpha(E)$ curve.

Samples of Ge suitable for high-temperature studies in the solid and liquid phases have been prepared from mixtures of Ge and inert matrix powder as described elsewhere [14]. We have used high-purity 99.9995% graphite powder and 99.95% BN. Ge K-edge spectra have been measured with negligible resolution broadening as a function of temperature. The near-K-edge spectra of solid Ge at 330 K and liquid Ge at 1370 K are reported and

compared in figure 3. These spectra are similar to those previously reported [14] but of better quality. Melting is accompanied by a dramatic change in the spectrum, with an evident shift of the edge to lower energy by 1.3 eV, with respect to the room temperature data, reflecting the disappearance of the energy gap in the semiconductor-to-metal transition. The height of the first resonance increases and the fine structure is smoothed into a relatively flat background as a consequence of the increased disorder. The difference spectrum $\Delta\alpha$ is reported in figure 3 on the same scale, indicating that selected energy points have an absorption discontinuity of the same order of magnitude as the edge jump. The most sensitive energy point is at the threshold (the vertical arrow at $E \approx 11.101$ keV) and mainly reflects the metallization transition. Energy points sensitive to structural transformations are found in the fine-structure region instead.

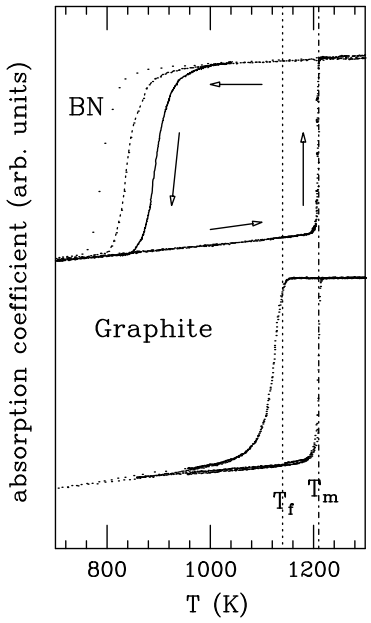

Figure 4. X-ray absorption hysteresis loops detected at fixed energy and obtained by cycling the temperature above and below T_m. The upper curves refer to Ge dispersed in BN; the large undercooling phenomenon depending on the cooling rate is quite evident. The rates are 0.05 K s^{-1} (solid line), 8 K s^{-1} (dashed line), 50 K s^{-1} (dotted line). The lower curve refers to Ge dispersed in graphite. A sudden freezing transition is observed in this case at $T_f \approx 1140$ K (vertical dotted line) as a consequence of some form of interaction occurring between Ge and graphite particles.

The previous investigation [14] has clearly shown the possibility of substantially undercooling liquid Ge. The observed differences in behaviour between BN and graphite matrices are demonstrated more deeply in this study. We performed a large number of experiments on Ge samples embedded in BN and graphite matrices. Particular care was devoted to the temperature homogeneity and calibration, which was simultaneously measured by a chromel–alumel thermocouple and a pyrometer. In the absence of impurities and for a wide range of particle size we obtained reproducible results. In figure 4 we report typical hysteresis curves $\alpha(T)$ obtained at $E = 11.101$ keV for Ge embedded in BN and graphite. The upstroke is similar for the two cases: there is a linear increase of absorption in the solid phase due to a linear edge shift associated with the effect of the

electron–phonon interaction on the density of unoccupied states [15]. At $T_m = 1210$ K the absorption suddenly increases to the liquid value remaining basically constant over a relatively wide temperature range. This corresponds to the absorption of metallic Ge.

The normal pattern observed in the upstroke is not reversible in the downstroke, indicating the possibility of undercooling the samples and clearly shows the different behaviours of the BN and graphite matrices. For BN, $\alpha(T)$ remains at the level of α_L down to 900 K and then starts to curve down to the α_S-value. The slope of the curve indicates a spread of the freezing of the various droplets in the sample, perhaps following impurity or size distribution. The freezing temperature was also found to be dependent on the cooling rate. The three curves reported in figure 4 for BN correspond to cooling rates of 50 K s^{-1}, 8 K s^{-1}, 0.05 K s^{-1} for which undercooling ranges of ∼400 K, ∼350 K, and ∼300 K below T_m were reached, respectively. These results confirm the previous x-ray absorption findings [14] and conform to the observed behaviour for isolated Ge droplets [16].

In the case of graphite, however, a sharper decrease of absorption is observed at $T_f = 1140$ K which can only be attributed to a sudden freezing of most of the Ge droplets. This freezing temperature is found to be largely independent of the cooling rate.

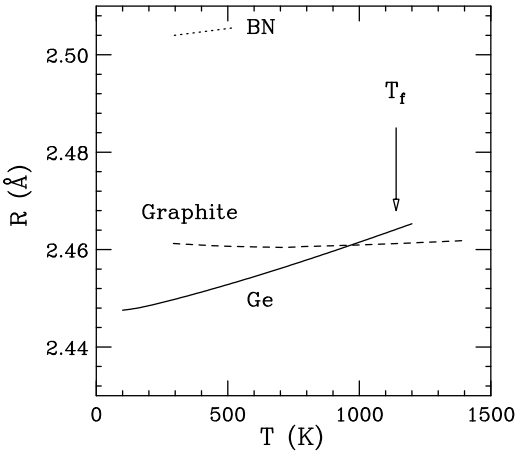

Figure 5. The temperature variation of the Ge–Ge bond length in c-Ge and of the second-neighbour distances in the hexagonal planes of BN and graphite. The different thermal expansions of the crystals bring the Ge and graphite distances into coincidence at $T \approx 1000$ K. This is relatively close to T_f where the freezing of the undercooled Ge/graphite samples is observed.

An explanation for such peculiar behaviour can be sought in the effects of the Ge/matrix interactions. Both BN and graphite are immiscible with Ge, but it is known that the presence of foreign particles can stimulate the crystallization. A mechanism for this phenomenon can be associated with the close matching of the c-Ge bond length with some characteristic distance in the matrix. To support this interpretation we report in figure 5 the calculated Ge–Ge bond length as a function of temperature [14] and the corresponding (practically constant) value for the second neighbours on the graphite and BN hexagonal planes. There is a close matching between the temperatures at which the graphite and Ge bond lengths intersect with T_f. Thus we propose that freezing is in this case stimulated by the periodic potential on the graphite planes on a wetting Ge layer, when the temperature is lowered to a value for which the formation of a covalent bond cannot be avoided. Further investigations on the Ge/graphite interactions are stimulated by these findings.

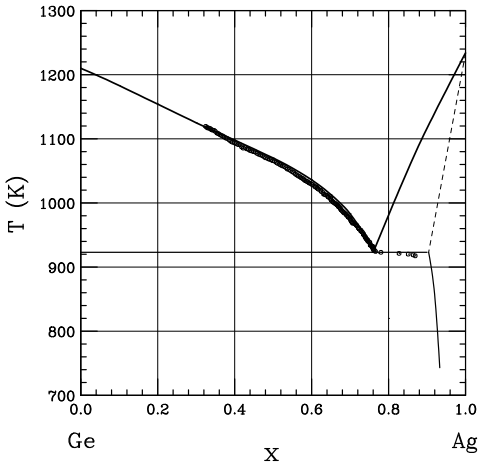

Figure 6. The phase diagram of the $Ge_{1-x}Ag_x$ alloy. The liquidus curve obtained from the single-energy temperature scan for the sample at $x = 0.30$ is reported as a dotted line. The close matching between known and measured curves supports our present interpretation of the measurements of binary alloys with eutectic phase diagrams.

4.3. Melting of binary alloys

From the phenomenological point of view, melting of binary alloys is a rather complicated phenomenon. We will limit our discussion to alloys characterized by a simple eutectic phase diagram with the elements fully miscible only in the liquid phase and a minimum of the melting curve at T_e corresponding to the eutectic composition x_e. An example of these alloys is Ge–Ag whose phase diagram [17] is reproduced in figure 6. An alloy sample $Ge_{1-x}Ag_x$, of average nominal composition x, can be obtained by mixing precursor powder of the two components and by heating to high temperature for a sufficient time. The sample is stabilized by successive heating and cooling cycles. In the liquid phase it is formed by droplets of the macroscopic sample composition x. Fluctuations in the composition between different droplets are eliminated by the diffusion which occurs especially at high temperature throughout the whole pellet. At low temperature each droplet freezes into the mixture of the stable solid phases, namely Ge and Ag:Ge. Most of the Ge is in the semiconducting solid phase, so a Ge K-edge study at 11.101 keV provides the most sensitive measure of the Ge melting.

We performed a single-energy experiment on a sample with $x = 0.30(1)$ and the measured hysteresis curve is reported in figure 7. With respect to the pure Ge case (figure 4) the upper stroke now shows a complicated behaviour with two major absorption discontinuities. The large hysteresis loop occurring in the downstroke indicates that the molten alloy can also be undercooled well below T_e. This is peculiar to Ge and is due to the substantial undercooling observed in the pure case. A qualitative explanation of the main features in the upstroke is obtained by assuming that the absorption coefficient reflects the percentage of metallized (i.e. molten) Ge atoms. This fraction increases with temperature in a discontinuous way reflecting the phase transitions occurring in the phase diagram of the alloy.

A quantitative interpretation can be also given. The concentration $x = 0.30$ lies on the left-hand side of the eutectic composition $x_e = 0.741$ (figure 6). Let the liquidus curve be described by the function $T_m = \theta(x)$ for $x < x_e$, which we suppose invertible

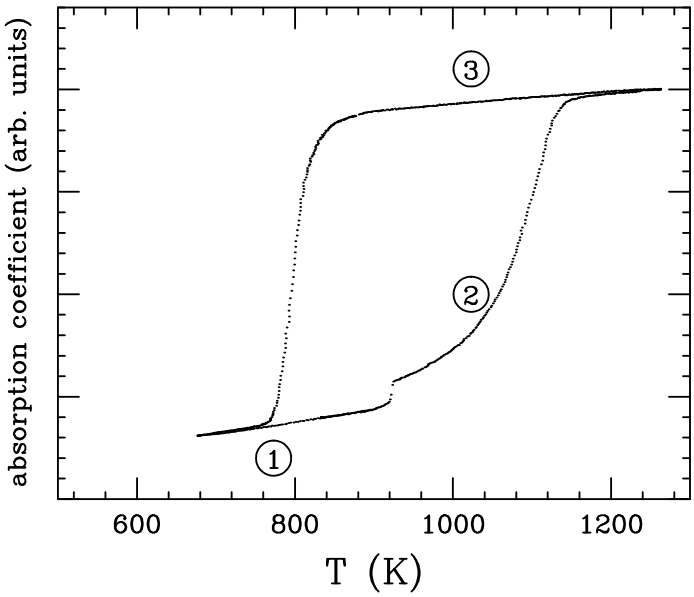

Figure 7. The single-energy absorption curve for $Ge_{0.7}Ag_{0.3}$. The eutectic melting at $T_e = 923$ K and the successive gradual increase of the absorption, due to the gradual increase of the sample molten fraction, up to the actual alloy melting point are quite evident. Regions 1, 2 and 3 refer to the quantitative model reported in table 1 and described in the text.

Table 1. The sample composition and total absorption as functions of temperature. The actual molten alloy composition y in region 2 is determined by the melting curve as $y = \theta^{-1}(T)$.

Region	Temperature	Stable phases	Sample fraction	Ge fraction	Absorption
1	$T < T_e$	Solid Ge	$1 - \dfrac{x}{1-\epsilon}$	$\dfrac{1}{(1-x)}\left(1 - \dfrac{x}{1-\epsilon}\right)$	$\alpha_S(T)$
		Solid $Ag_{1-\epsilon}Ge_\epsilon$	$\dfrac{x}{1-\epsilon}$	$\dfrac{\epsilon x}{(1-\epsilon)(1-x)}$	$\alpha_a(\epsilon, T)$
2	$T_e < T < \theta(x)$	Solid Ge	$1 - \dfrac{x}{y}$	$\dfrac{1}{(1-x)}\left(1 - \dfrac{x}{y}\right)$	$\alpha_S(T)$
		Molten Ag_yGe_{1-y}	$\dfrac{x}{y}$	$\dfrac{x(1-y)}{y(1-x)}$	$\alpha_L(y, T)$
3	$T > \theta(x)$	Molten Ag_xGe_{1-x}	1	1	$\alpha_L(x, T)$

as $x = \theta^{-1}(T_m)$. We distinguish three temperature regions as described in table 1 and indicated in figure 7. At low temperature, $T < T_e$, the stable phases are pure solid Ge and solid Ag:Ge with a small Ge impurity concentration ϵ. At T_e all of the Ag atoms melt with an appropriate fraction

$$f = \frac{1 - x_e}{x_e}\frac{x}{1-x}$$

of the total Ge atoms to reach the eutectic melt composition. Between T_e and $\theta(x)$ the stable phases are solid Ge and the molten alloy $Ge_{1-y}Ag_y$. The concentration is given by

the liquidus curve, namely $y = \theta^{-1}(T)$, which decreases with increasing temperature. This implies the gradual melting of the remaining solid Ge particles and the corresponding rise of the absorption coefficient. Above $T = \theta(x)$ the sample is single phase: it is a homogeneous molten $Ge_{1-x}Ag_x$ alloy. The molar fractions of the stable phases, the fraction of Ge atoms in each phase, and their absorption coefficients, are indicated in table 1. At the Ge K edge the Ag absorption cross-section is independent of the phase and therefore this trivial constant contribution can be neglected. Consequently we can write the x-ray absorption coefficient for the three regions as

$$\alpha_1(T) = \frac{\epsilon x}{(1-\epsilon)(1-x)}\alpha_a(\epsilon, T) + \frac{1}{(1-x)}\left(1 - \frac{x}{1-\epsilon}\right)\alpha_S(T) \tag{5a}$$

$$\alpha_2(T) = \frac{x(1-y)}{y(1-x)}\alpha_L(y, T) + \frac{1}{(1-x)}\left(1 - \frac{x}{y}\right)\alpha_S(T) \tag{5b}$$

$$\alpha_3(T) = \alpha_L(x, T) \tag{5c}$$

where the phase- and temperature-dependent Ge atomic absorption cross-sections are indicated by $\alpha_S(T)$, $\alpha_a(\epsilon, T)$ and $\alpha_L(x, T)$ for solid Ge, Ge in solid Ag:Ge and Ge in the molten alloy, respectively. The combination of these three expressions results in a piecewise-continuous curve with a discontinuity at T_e and a discontinuity in the first derivative at $\theta(x)$. The absorption change in the intermediate region is due, in principle, to both increased quantity and compositional change of the molten fraction which may affect $\alpha_L(y, T)$. The temperature dependence of $\alpha_S(T)$ has already been discussed.

A simplified expression can be obtained with the assumption that at the Ge K edge $\alpha_a(\epsilon, T) = \alpha_L(x, T) = \alpha_M$ where α_M is a generic metallic germanium absorption. Then the absorption coefficient can be described by the single equation

$$\alpha(T) = \frac{1}{(1-x)}\alpha_S(T) + \frac{x}{y(1-x)}\left[(1-y)\alpha_M - \alpha_S(T)\right] \tag{6}$$

where the absorption changes are due to the variations of the alloy concentration y in the second term. At low temperature, $y = 1 - \epsilon$; at T_e, y is suddenly reduced to x_e and then it gradually decreases to x at $\theta(x)$.

Equations (5) can be used in different ways. If the melting curve is known to a high degree of accuracy the value of the absorption coefficient for the liquid phase can be obtained as a function of the composition which changes with temperature:

$$\alpha_L(y) = \frac{y(1-x)}{x(1-y)}\alpha(T) - \left(\frac{y}{x} - 1\right)\frac{1}{(1-y)}\alpha_S(T) \tag{7}$$

and conversely if the absorption coefficient for the molten phase is known (or assumed known, possibly having a constant value α_M) the liquidus curve in the interval $x < y < x_e$ can be obtained:

$$y(T) = \frac{x[\alpha_M - \alpha_S(T)]}{[(1-x)\alpha(T) - \alpha_S(T) + x\alpha_M]}. \tag{8}$$

In both cases the analysis of the temperature scan of a single sample provides interesting information on a continuous range of melt compositions.

In the present case $\alpha_S(T)$ is not directly measured; however, it can be calculated from the absorption coefficient in region 1 as given by equation (5*a*) as

$$\alpha_S(T) = \alpha_1(T)(1+\eta) - \eta\alpha_M \tag{9}$$

where

$$\eta = \frac{x\epsilon(T)}{1 - x - \epsilon(T)}. \tag{10}$$

We have used the known solubility $\epsilon(T)$ of Ge in Ag [17] and the extrapolated values of the absorption coefficient measured in regions 1 and 3. In all cases a linear temperature dependence was assumed. The experimental liquidus curve that is obtained using these approximations is reported in figure 6 and is found to be in excellent agreement with the known curve. In the present case we believe that the composition dependence of the absorption coefficients is negligible because it is only reflecting whether Ge is in a semiconducting or metallic phase.

This example shows the degree of insight that can be obtained into binary alloys using our single-energy technique. Several applications can be foreseen, including the detection of anomalies of electronic or structural properties as a function of the composition and the measurements of the liquidus curve at high pressure. Moreover, for alloy samples, this scanning procedure is essential for establishing whether the corresponding EXAFS spectrum can be interpreted as originating from a single phase or not. Our results indicate that the molten alloy can be studied over a wide range of temperatures from the undercooling to the evaporation limit.

4.4. Melting in the presence of impurities

For a large class of binary alloys the melting points of pure substances are lowered by the addition of foreign elements. When these atoms are present in the low-concentration limit $x \approx 0$ we can approximate the corresponding alloy liquidus curve by a linear function $\theta(x) = T_m^0 - \beta x$. The effect on the melting curve can be calculated using equation (6) by putting $y = (T_m^0 - T)/\beta$ and neglecting all first-order terms in x besides those in $1/y$ which are diverging towards the melting point of the pure substance T_m^0, which gives

$$\alpha(T) = \alpha_S(T) + \frac{x\beta}{T_m^0 - T}[\alpha_L - \alpha_S]. \tag{11}$$

This equation indicates that, in the presence of impurities, the absorption discontinuity at melting is rounded as an inverse function $b/(T_m^0 - T)$ where $b = x\beta$ is the product of the concentration and the slope of the melting curve for the alloy with the given impurity. In practice a small fraction of the sample still melts at T_e but it is usually too small to be detected. Melting around the impurities proceeds and involves a macroscopic fraction of the samples only very close to T_m^0. Typical values of β are in the range 100–500 K so, even for concentrations in the 10^{-5} range, $b \approx 10^{-2}$. In the case of high sensitivity to melting in the 10^{-3} range, like for Ge, the absorption curve has already departed visibly from the pure-substance limit 10 K below T_m^0. Thus impurities appear to be dominant among the factors causing the rounding of the melting onset in most cases.

A typical pellet is composed of a mixture of 10–20 mg of sample with 100–500 mg of inert matrix. Typical atomic fractions are 1:50 which means that every impurity in the matrix is amplified by a factor of 50 if it alloys with the sample. In order to keep the final impurity concentration below 10^{-3} it is necessary to use a matrix of extremely high purity, possibly better than 99.999% and to work in a clean environment to avoid contamination by more than about 10 μg of foreign matter.

We point out for comparison that in the EXAFS of the majority atoms, impurities below 1% can hardly be detected by their structural signature. Thus the sharpness of melting is a rigorous test of overall sample purity as far as structural measurements are concerned.

In order to illustrate the impurity melting phenomenon, the absorption curves $\alpha(T)$ can be plotted as functions of the inverse of the molten fraction f:

$$1/f = \frac{\alpha_L - \alpha_S(T)}{\alpha(T) - \alpha_S(T)} = \frac{T_m^0 - T}{x\beta}. \tag{12}$$

$\alpha_S(T)$ and α_L can be approximated by linear functions interpolated in the appropriate regions of the curve. In the case of impurity melting, the first term of equation (12) versus T must show a linear behaviour whose slope is inversely proportional to the impurity concentration times β. In the case of the presence of more impurity species, one can directly assume an additive effect leading to a slope equal to $-1/\sum x_i\beta_i$.

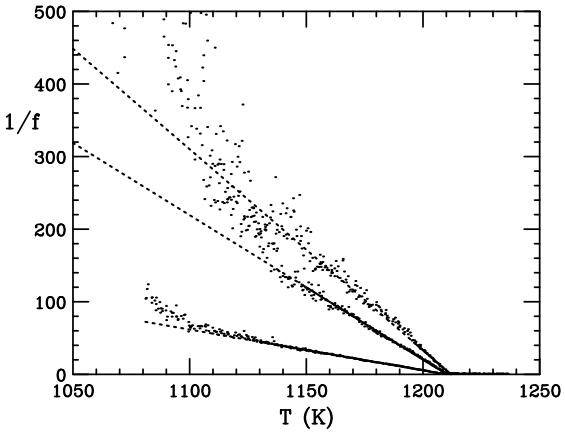

Figure 8. Impurity melting effects from three different Ge samples demonstrated by plotting the inverse molten fraction $1/f$ as a function of T. The linear behaviour close to T_m^0 indicates a $1/(T_m^0 - T)$ divergence of the absorption coefficient.

Experimental examples of the effect of impurities in the case of Ge in BN are shown in figure 8 for different impurity levels. The rounded melting pattern cannot be generated by artifacts due to temperature homogeneity and their impurity origin is confirmed by this graphical treatment in which the characteristic -1 power-law behaviour is apparent.

4.5. Non-bulk phenomena

In addition to experimental artifacts or impurities, the sharp bulk melting behaviour can be modified by the presence of non-bulk components. Samples are normally formed by small particles/droplets with a diameter in the 1 μm range. These are still macroscopic samples as far as the thermodynamical and microscopic properties are concerned. As the diameter is lowered down to the cluster range the individual particles are too small to be treated in the thermodynamic limit and the notion of phase transitions is not valid any longer. As is usually found by molecular dynamics simulation of clusters, atom mobility increases with temperature and the structure fluctuates between different low-energy configurations [18]. Correspondingly, a smoothed variation occurring over a wide range of temperatures is substituted for the derivative discontinuity in the thermodynamic potentials. For these systems the corresponding melting pattern is expected to be smeared out into a smoothed discontinuity.

Between the bulk and the cluster regimes an intermediate situation can be identified where the particles are still big enough to possess sharp phase transitions, as in the

thermodynamic limit, but where the percentage of the surface component increases and becomes observable. This occurs well above the nanometre scale characteristic of the small-particle behaviour. To give a figure, we can estimate that for a spherical particle that is $2R = 1$ μm in diameter, a $d = 1$ nm surface layer already contributes with a macroscopic volume percentage equal to $f = 3d/R \approx 0.6\%$ which is above the detectability limit.

Surfaces on their own undergo phase transitions distinct from the bulk ones, including reconstruction, order–disorder transitions and melting. In particular surface melting [19] has attracted much attention in recent times. It has been observed for several low-index surfaces of metals [20] and is thought to be a rather general phenomenon initiating the melting of pure solids. In the Ge(111) case the high-temperature disordering transition at ≈1050 K has been described as an incomplete surface melting case [21]. The theory of surface melting [19, 20] predicts a logarithmic (or low-fractional-power) divergence of the molten layer as T approaches T_m. In the single-energy experiment one does not directly measure the thickness of the surface layer, but only the molten atomic fraction. However, under very general conditions it can be demonstrated (see the appendix) that the atomic fraction involved in a molten surface layer of thickness d is directly proportional to d, for a wide range of thicknesses, independently of the microscopic details of the matter distribution. In the presence of a diverging molten surface layer one should, therefore, observe a corresponding divergence of α_S towards α_L at T_m with the same functional relationship. We conclude that surface melting might be observed as a rounding of the melting onset just like in the impurity case. We point out, however, that the -1 power law of the impurity melting is eventually going to dominate close to T_m over any possible surface melting effect, which should be characterized by a weaker divergence. As a consequence, in those cases in which surface effects are visible we predict the observation of a crossover to the impurity melting behaviour in the $\alpha(T)$ curve close to T_m.

Impurity and surface melting appear to be competing phenomena in the rounding of melting patterns. In this work the rounding of the Ge melting curves has been interpreted as impurity melting; however, the present calculations indicate that the surface and impurity effects in the 10^{-3} range can be competing. A possible way of discriminating between the two effects is on the basis of the different functional behaviours.

Further investigations are required to fully understand the potential of the technique for identifying and studying surface effects. One clear disadvantage is that our samples cannot be characterized from the surface physics point of view. They contain in general a large number of different surfaces, possibly confined by small lateral extension which might modify their behaviour from the infinite-surface case commonly considered. Moreover, surface effects and impurity effects are clearly not easily distinguishable with a volume-sensitive technique for which the surfaces can be regarded as ‘impurities’ of the bulk just like foreign atomic species.

5. Conclusion

New installations at third-generation synchrotron radiation sources have permitted the development of novel x-ray absorption experiments and previously unexploited techniques like single-energy x-ray absorption detection as a function of sample environment parameters. In this paper we have described the instrumentation available at ESRF-BM29 which allows temperature scans with a closed-cycle He cryostat in the range 20–400 K and with a high-temperature oven in the range 300–3000 K.

The general principles of single-energy x-ray absorption detection as a probe for phase transitions in condensed matter are formulated and specific cases of first-order

phase transitions are discussed. Most of the examples are related to melting which is a representative example of these transformations for which a large number of experimental data have been collected. The case of binary alloys has been treated and a general formulation able to explain the main features of the observed pattern has been provided. Finally we have demonstrated the high sensitivity to departures from the ideal behaviour including undercooling phenomena and impurity melting, and we have discussed the possible signatures for non-bulk effects like cluster or surface melting.

Clearly these examples do not exhaust all of the possible studies. Thermal treatment can activate chemical reactions, reversible or non-reversible in nature, and single-energy absorption can be a method for studying the phenomena with a time resolution of the order of 0.1–1 s with a very high sensitivity.

Yet, several other applications can be foreseen combined with the scanning of a different sample environment parameter, like pressure, magnetic field or pH, which stimulate the development of several other automated control systems.

Single-energy temperature scans are an essential tool to be combined with traditional XAS for characterizing *in situ* the nature of the sample and for preparing it in a precise phase. They can provide an independent check of sample purity and nature, and can be used to prepare the sample in a given non-equilibrium state and to confirm its stability during acquisition of complete EXAFS spectra. In this respect the technique that we have developed becomes an important characterization technique to be incorporated in an XAS facility.

The examples presented have shown that even in the case of well understood phase transitions, like the melting of pure substances, novel information can be obtained for instance on the undercooling phenomenon. Of course, phase transitions are normally characterized by differential scanning calorimetry (DSC) or temperature-dependent x-ray diffraction patterns, and our method is not a substitute for these techniques. Instead, it is largely complementary and can provide novel insight into phase transitions, as can be understood by considering the following remarkable characteristics: (a) the local order sensitivity combined with the atomic selectivity, (b) the photon tunability for selecting electronic or structural sensitivity and (c) the access to a direct structural probe (EXAFS) at the same installation.

Also, with respect to diffraction, apart from the obvious advantage as regards the number of photons directly available for absorption measurements with respect to the diffracted ones, our technique has the advantage of being extremely accurate in determining the atomic fraction in a selected phase and of being applicable also to phase transformations into disordered systems. All of these examples illustrate the potential of the method for investigating phase transitions in condensed matter.

Acknowledgments

We acknowledge J Jensen (formerly at ESRF) for his invaluable technical help. All of the beamtime was on BM29 at the ESRF, under proposals HC-517 and MI-124.

Appendix. The atomic fraction of the molten surface layer

In order to understand the possible effect of a growing molten surface layer on the $\alpha(T)$ curve close to melting we require an estimate of the atomic molten fraction as a function of the surface layer thickness d. For simplicity we neglect the density differences between the

solid and liquid and calculate volume fractions instead. In the limit of small d with respect to typical particle size, the linear relation $f \approx d\Sigma/V$ holds, where Σ is the total area of the melting surface and V is the sample volume. This equation breaks down when two melting layers from equivalent surfaces come into contact yielding a negative second-order term. Let R be the average radius of the crystallites and d be the thickness of the molten layer. By dimensional arguments, the fraction of molten volume for a single particle will be $f = 1 - (R - \gamma d)^3/R^3$ for $\gamma d \leqslant R$. The dimensionless constant γ depends on the specific shapes and extension of the melting surfaces. In the case of regular polyhedra or a sphere, $\gamma = 1$; in any case γ is just a proportionality constant and will be omitted in the following. In the real case there will be a size distribution associated with the original powder fragmentation and selection. Let us indicate as $p(r), r \geqslant 0$, the normalized probability density of the average particle radii r. The molten volume fraction f is given by unity minus the solid fraction and is approximated by

$$f \approx 1 - \int_d^\infty (r-d)^3 p(r)\ \mathrm{d}r \left[\int_0^\infty p(r) r^3\ \mathrm{d}r\right]^{-1}$$
$$= \frac{1}{\mu^{(3)}}\left(3d\mu^{(2)} - 3d^2\mu + d^3 - \int_0^d (d-r)^3\ p(r)\ \mathrm{d}r\right). \tag{A1}$$

This expression can be evaluated exactly for model distributions, but a careful analysis reveals that the leading non-linear terms are largely independent of the details of the particle distribution. They depend in fact only on integral properties like ratios of nth moments of the size distribution with respect to $r = 0$ (indicated as $\mu^{(n)}$).

The last integral deserves some discussion. The integration limit d originates from the fact that particles smaller than d are completely molten; this is strictly valid for spherical particles. Irrespective of $p(r)$, the resulting $f(d)$ is uniformly continuous with its first derivative, at least. If $p(r)$ is analytic it is possible to obtain a Taylor expansion with respect to the parameter d, for $d = 0$. Due to the integration limits and the third power $(d-r)^3$, the first non-vanishing derivative is the fourth one yielding a small corrective term $d^4 p(0)$. In the general case we find the upper bound

$$\int_0^d (d-r)^3 p(r)\ \mathrm{d}r < d^3$$

which indicates that the last integral is always smaller than the cubic term of the power expansion. In practice the effect of the last integral is negligible as far as the linearity of the relation $f(d)$ is concerned. This result indicates that the departure from a linear relation between d and f is largely independent of the details of the particle distribution and depends only on average properties expressed by the moment ratios.

The second-order correction coefficient in dimensionless units equals $-\frac{1}{3}\mu^{(3)}\mu^{(1)}/(\mu^{(2)})^2$ and it is always less than 1 for a large class of realistic particle size distributions. This means that over the whole range up to $f \sim 0.2$–0.3, the measured $f(T)$ curve can be directly interpreted as a quantity proportional to the thickness of the surface layer $d(T)$, apart from an unknown sample-dependent conversion constant.

References

[1] Als-Nielsen J, Grübel G and Clausen B S 1995 *Nucl. Instrum. Methods Phys. Res.* B **97** 522
[2] Frahm R 1988 *Nucl. Instrum. Methods Phys. Res.* A **270** 578
Frahm R 1989 *Rev. Sci. Instrum.* **60** 2515
[3] Hagelstein M, San Miguel A, Fontaine A and Goulon J 1997 *Proc. 9th XAFS Conf.; J. Physique Coll.* IV at press

[4] Frahm R, Wong J, Holt J B, Larson E M, Rupp B and Waide P A 1992 *Phys. Rev.* B **46** 9205
[5] Goulon J, Brookes N B, Gauthier C, Goedkoop J, Goulon-Ginet C, Hagelstein M and Rogalev A 1995 *Physica* B **208 + 209** 199
[6] Filipponi A and Di Cicco A 1994 *Nucl. Instrum. Methods Phys. Res.* B **93** 302
[7] Besson J M, Nelmes R J, Hamel G, Loveday J S, Weill G and Hull S 1992 *Physica* B **180 + 181** 907
[8] Filipponi A 1996 *J. Phys.: Condens. Matter* **8** 2335
[9] Hultgren R H, Desai P D, Hawkins D J, Gleiser M, Kelley K K and Wagman D D 1973 *Selected Values of the Thermodynamic Properties of the Elements* (Metals Park, OH: American Society of Metals) p 630
taken from
Landolt–Börnstein New Series 1994 Group III, vol 19i1 (Berlin: Springer) §7.1.1.2, p 3
[10] Basinski Z S, Hume-Rothery W and Sutton A L 1995 *Proc. R. Soc.* A **229** 459
[11] Wangsgard A P 1942 *Trans. ASM* **30** 1303
[12] Couture A and Angers R 1986 *Metall. Trans.* A **17** 37
[13] Takasaki A, Ojima K and Taneda Y 1995 *Phys. Status Solidi* a **148** 159
[14] Filipponi A and Di Cicco A 1995 *Phys. Rev.* B **51** 12 322
[15] Lautenschlager P, Allen P B and Cardona M 1985 *Phys. Rev.* B **31** 2163
[16] Devaud G and Turnbull D 1987 *Acta Metall.* **35** 765
[17] *Landolt–Börnstein New Series* 1987 Group IV, vol 5a (Berlin: Springer) p 46
[18] Honeycutt J D and Andersen H C 1987 *J. Phys. Chem.* **91** 4950
[19] Tosatti E 1988 *The Structure of Surfaces II* ed J F van der Veen and M A Van Hove (Berlin: Springer) p 535
[20] Frenken J W M, Marée P M J and van der Veen J F 1986 *Phys. Rev.* B **34** 7506
Denier van der Gon A W, Smith R J, Gay J M, O'Connor D J and van der Veen J F 1990 *Surf. Sci.* **227** 143
[21] Denier van der Gon A W, Gay J M, Frenken J W M and van der Veen J F 1991 *Surf. Sci.* **241** 335
Takeuchi N, Selloni A and Tosatti E 1994 *Phys. Rev. Lett.* **72** 2227